Journal of The Electrochemical Society, **161** (3) H105-H113 (2014)
0013-4651/2014/161(3)/H105/9/$31.00 © The Electrochemical Society

Influence of Trivalent-Dopants on the Structural and Electrochemical Properties of Uranium Dioxide (UO_2)

Mayuri Razdan[a,*] and David W. Shoesmith[a,b,,z]**

[a]*Department of Chemistry, Western University, London, Ontario N6A 5B7, Canada*
[b]*Surface Science Western, London, Ontario N6G 0J3, Canada*

The influence of trivalent dopants (rare-earths, RE) on the structure, composition and electrochemical reactivity of UO_2 has been investigated using scanning electron microscopy (SEM/XRD), X-ray photoelectron spectroscopy (XPS), Raman spectroscopy and cyclic voltammetry (CV). This was achieved by comparing the behavior of undoped $UO_{2.002}$, a slightly doped 1.5 at% SIMFUEL, and two rare-earth doped UO_2 (6 wt% Gd-UO_2 and 12.9 wt% Dy-UO_2) specimens. The reactivity decreased in the order $UO_{2.002}$ > SIMFUEL > Dy-UO_2 > Gd-UO_2, showing that this decrease is a consequence of RE^{III} doping. Raman spectroscopy showed this could be attributed to the formation of RE^{III} – oxygen vacancy clusters whose formation decreases the availability of the vacancies required to accommodate the injection of oxygen interstitials during anodic oxidation. The behavior of SIMFUEL is complicated by the simultaneous formation of RE^{III}- oxygen vacancy clusters and Zr-O_8 clusters.
 [DOI: 10.1149/2.047403jes]

Manuscript submitted November 7, 2013; revised manuscript received December 16, 2013. Published December 27, 2013.

The safe disposal of spent nuclear fuel (SNF) is one of the key issues facing the modern nuclear power industry, and a major international effort is underway to develop safe management and disposal procedures. One potential management strategy in Canada is permanent disposal in a deep geologic repository.[1] The spent fuel would be sealed in metallic containers, emplaced in a repository and surrounded with compacted clay. The prospects for long term containment using copper containers are very good and corrosion models predict only minimal corrosion damage should be sustained.[2,3] However, if failure were to occur, contact of the fuel wasteform (uranium dioxide (UO_2)) with groundwater would become possible. Although the solubility of UO_2 is very low under the anticipated anoxic conditions, radiolysis of the groundwater, due to the inherent radioactivity of the spent fuel, could lead to fuel corrosion, the U(IV) in the fuel being oxidized to the significantly more soluble U(VI) state.[4] This would make radionuclide release to the groundwater possible.

Spent fuel is mainly UO_2 (> 95%), the remainder being the radioactive fission products and actinides produced during the in-reactor process. The inventory of radionuclides within the fuel depends on in-reactor burn-up and the linear power rating of the fuel.[5] Formation of these products leads to many physical and chemical changes within the fuel,[5] and post irradiation inspection of the fuel shows the presence of both volatile and non-volatile fission products. While volatile products may escape to the fuel-cladding gap, the non volatile products remain fixed within the fuel matrix in three distinct phases: the lanthanides in the fcc-fluorite lattice; the noble metals in metallic precipitates; and radionuclides unstable in the fluorite matrix in mixed metal oxides (perovskites).[6]

The key changes likely to influence the chemical reactivity of the UO_2 matrix are the rare earth (RE) doping of the matrix and the development of non-stoichiometry.[7] Micro Raman spectroscopic studies show that non-stoichiometry leads to very significant changes in fuel structure as x (in UO_{2+x}) increases.[8] Close to stoichiometry there is an increase in randomly distributed O interstitial defects as x increases. As the degree of non-stoichiometry increases further these defects associate into clusters, and for a sufficiently high degree of non-stoichiometry cuboctahedrals clusters are formed.[8,9] Studies using atomic force microscopy (AFM), current sensing AFM and scanning electrochemical microscopy clearly demonstrate that the fuel reactivity increases as the extent of defect clustering increases.[7] While the exact anodic oxidation mechanism remains to be resolved, the extent of oxidation on a surface close to stoichiometric appears to be limited by the low O interstitial (O_I) mobility within the matrix. At higher degrees of non-stoichiometry the formation of defect clusters enhances O_I mobility in the matrix facilitating a deeper and more extensive surface oxidation.

Considerable experimental evidence exists to show that fission product and actinide-lanthanide doping have a significant effect on the kinetics of air oxidation of the fuel,[10–13] and preliminary electrochemical experiments on SIMFUEL suggest a similar influence in aqueous environments.[6] Since there has been a continuous trend toward higher in-reactor fuel burn-up,[14–16] the extent of doping and its influence on reactivity are becoming more important. Both the mechanism and the rate of oxidation are influenced by the presence of dopants. The reaction proceeds in two stages

$$UO_2 \rightarrow U_4O_9/U_3O_7 \rightarrow U_3O_8 \qquad [1]$$

The first step involves the diffusion of O through the growing surface oxidized layer of either U_4O_9 (O:U = 2.25 to 2.4) or tetragonal U_3O_7 (O:U = 2.33), while the second step involves a recrystallization via a nucleation and growth mechanism to the orthorhombic U_3O_8.[10]

A key feature of this oxidation process is that the nature of the intermediate phase changes as the doping level is increased. For pure, or lightly doped, UO_2 oxidation occurs relatively rapidly to the tetragonal U_3O_7 and the subsequent conversion to orthorhombic U_3O_8 is easily completed. However, the oxidation of UO_2 containing large amounts of dopants (such as Gd) is kinetically slower and proceeds through U_4O_9 which retains the fluorite structure and is kinetically more difficult to transform to U_3O_8. These observations are supported by a range of studies with SIMFUELs,[17,18] LWR fuels (highly doped)[19] and CANDU fuels (lightly doped).[20]

Park and Olander[21,22] offered an explanation for the stabilization of RE^{III}-doped UO_2 against oxidation based on O potential calculations, this potential being an indirect indicator of oxide-defect structure. A defect model for Gd-doped UO_2 was developed based on their original model for UO_2 which incorporated both intrinsic point defects and defect clusters. Experimental O potential data could be fitted by assuming Gd dopants existed mainly as isolated defects in the cation sublattice of the oxide. As the Gd content increased the Gd dopants were stabilized by the formation of dopant- oxygen vacancy clusters (O_V). This leads to a reduction in availability of the interstitial sites required for the incorporation of O_I during oxidation.

However, there is considerable evidence to show that the RE^{III}-doped matrix contains two distinct phases depending on the dopant content.[23–25] This separation into two phases is seen as a competition between O^V and U^V formation in order to ensure electroneutrality within the doped matrix.

In this study we have investigated the electrochemical reactivity of two RE^{III}-doped, an undoped and a SIMFUEL electrode, and correlated this reactivity to their oxide structures determined by Raman spectroscopy. SIMFUELs are UO_2 pellets doped with non-radioactive elements including rare earths (Ba, Ce, La, Sr, Mo, Y, Zr, Rh, Pd, Ru,

*Electrochemical Society Student Member.
**Electrochemical Society Active Member.
zE-mail:dwshoesm@uwo.ca

Nd) to replicate the chemical effects of in-reactor irradiation, and have been well studied electrochemically.[26] The RE^{III}-doped electrodes employed were doped with Gd (6.0 wt%) and Dy (12.9 wt%). While all rare earth dopants are not expected to have an identical effect on UO_2,[22] this comparison offers a first opportunity to determine their influence on the oxidative behavior of UO_2 in an aqueous environment.

Experimental

Electrode material and preparation.— Experiments were performed on a $UO_{2.002}$, 1.5 at% SIMFUEL, 6.0 wt% Gd_2O_3 (rare-earth) doped UO_2 (Gd-UO_2) and 12.9 wt% Dy_2O_3 (rare-earth) doped UO_2 (Dy-UO_2) electrodes. Fuel pellets of $UO_{2.002}$, SIMFUEL and Dy-doped UO_2 pellets were fabricated and supplied by Atomic Energy of Canada Limited (AECL, Chalk River, Canada) and the Gd-doped UO_2 by Cameco (Port Hope, Canada). All the pellets were sintered and reduced to produce high density stoichiometric ceramics. The pellets were cut into 2 mm thick slices and fabricated into electrodes using our previously published procedure.[27]

Electrochemical procedure.— Prior to experiments, electrodes were prepared by polishing on wet 1200 grit SiC paper and rinsed with distilled deionized water. Subsequently, the electrodes were electrochemically reduced at −1.2 V for 2 min (vs. SCE) to remove any air-formed oxides or organic contaminants present on the surface. Cyclic voltammetric experiments were performed by scanning the potential from −1.2 V to an anodic limit of ≤ 0.4 V and back at a scan rate of 10 $mV.s^{-1}$.

Solution preparation.— Solutions were prepared using distilled deionized water (resistivity (ρ) = 18.2 MΩ cm) purified using a Millipore Milli-Q plus unit which removes organic and inorganic impurities. Experiments were performed in 0.1 $mol.L^{-1}$ NaCl (Caledon) solution purged with Ar gas (Praxair). The solution pH was monitored with an Orion model 720A pH meter and adjusted to 9 using 0.1 $mol.L^{-1}$ NaOH.

Electrochemical cell and equipment.— A standard three-electrode, three-compartment cell was employed for all the experiments. The three compartments were separated by glass frits to avoid contamination of the working electrode. A Luggin capillary was used to minimize the ohmic potential drop due to solution resistance between the reference and working electrode. A Pt sheet (∼ 6 cm^2) spot-welded to a Pt wire was used as the counter electrode. A Solartron model 1287 potentiostat was used to control applied potentials and to record current responses. Corrware, version 3.0, software was used to analyze the data. The current interrupt method was employed to compensate for voltage drop due to ohmic resistance in the electrodes. All potential measurements were recorded against a saturated calomel reference electrode (SCE).

SEM/EDX measurements.— A Hitachi S-4500 Field emission scanning electron microscope (SEM) equipped with an energy dispersive X-ray (EDX) analyzer was used to collect images and determine elemental compositions. SEM micrographs were obtained on polished electrodes with the electron beam potential ranging from 10.0 kV to 15.0 kV according to requirements. The working distance was set at 10 mm during image collection. EDX mapping was used to determine the distribution of the dopants in the host UO_2 matrix. A number of randomly located areas of the surface were examined to determine whether the elemental composition was uniform.

Raman analysis.— All the Raman spectra were acquired using a Renishaw 2000 confocal Raman spectrometer (Renishaw PLC., UK). Raman active vibrations were excited on a UO_2 sample by a HeNe laser with a wavelength of 632.8 nm which produces a focused beam of about 2 μm diameter at the sample surface. The laser was used at 50% power to avoid any specimen heating effects since small changes in temperature can easily produce small changes in the frequency and width of Raman lines. The Raman spectrometer was calibrated using a Si crystal standard at room temperature. The laser beam was focused onto the sample using a Leica DMLM microscope with a 50x uncoated objective lens. Each spectrum was measured for an exposure time of ∼ 45 sec over the wavenumber range 120 to 1400 cm^{-1}. Repeated measurements were conducted at different locations on the electrode to ensure that bands do not show any shifts in vibrational frequency. After the measurement, the Gaussian-Lorentzian peak model and a Shirley baseline correction were used to fit the Raman peaks.

XPS analysis.— XPS spectra were recorded on a Kratos Axis Ultra spectrometer using an Al K_α (15mA, 14 kV) monochromatic high energy ($h\nu = 1486.6$ eV) radiation source. The instrument work function was set to give a value of 83.96 eV for the binding energy (BE) of the Au ($4f_{7/2}$) line of metallic Au. The spectrometer dispersion was adjusted to give a BE of 932.62 eV for the Cu $2p_{3/2}$ line of copper metal. Charge neutralization was used on all the specimens. The C 1s peak at 285.0 eV was used as a standard, to correct for surface charging, when required. All spectra were analyzed using CasaXPS software (version 2.3.14) and involved a 50% Gaussian and 50% Lorentzian fitting routine with a Shirley background correction. The procedure used to deconvolute the U4f spectra into contributions from U^{IV}, U^{V}, and U^{VI} has been described elsewhere.[28–31] The satellite structures close to the $U4f_{5/2}$ peak, and the valence band region were used to check the validity of the spectral fit.

Results

SEM/EDX analysis.— Figure 1 shows the surface morphology of polished 1.5 at% SIMFUEL, Gd-UO_2 and Dy-UO_2 electrodes at two

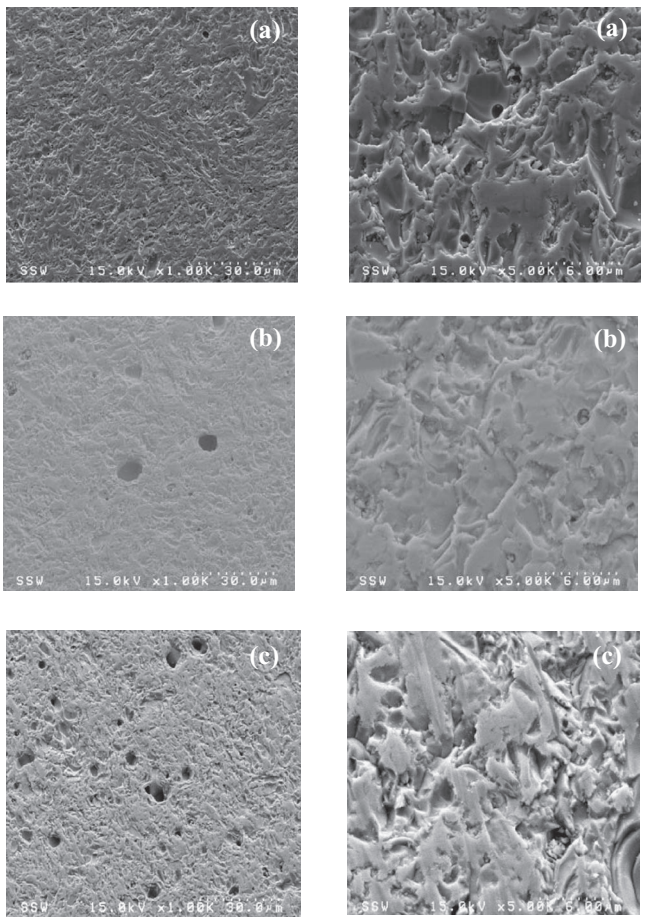

Figure 1. SEM micrographs recorded on a polished (a) 1.5 at% SIMFUEL (b) Gd-doped UO_2 and (c) Dy-doped UO_2 electrode at 1000 and 5000X.

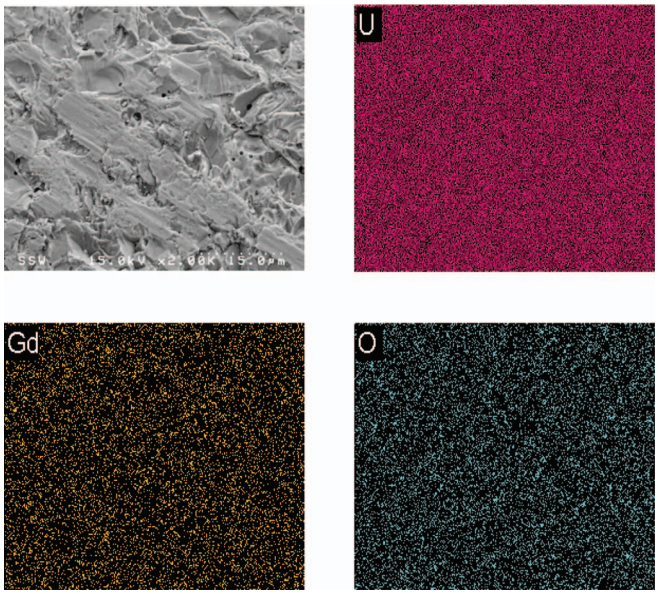

Figure 2. EDX maps recorded on a Gd-doped UO_2 at a magnification of 2000X.

magnifications. SEM images collected on the SIMFUEL micrographs show some porosity in the structure, Fig. 1a, which is commonly observed on the undoped $UO_{2.002}$.[7] SIMFUEL specimens have been characterized earlier in detail.[6,32,33] The Gd and Dy-doped UO_2 micrographs showed a similar porosity (Fig. 1b, 1c). EDX measurements were performed on a number of locations on the two rare earth doped electrodes, and representative patterns are shown in Figs. 2 and 3. As expected, EDX maps show a homogeneous distribution of the doping elements. No accumulation of Gd (as Gd_2O_3) or Dy (as Dy_2O_3) was observed. Also, analyses of randomly chosen locations confirmed that the Gd and Dy were both uniformly distributed as dopants in the UO_2 matrices. On this scale there is no evidence of the two phases observed by others.[23–25]

Surface electrochemistry.— Cyclic voltammetric (CV) experiments were conducted on each electrode to determine their electrochemical reactivity, especially their susceptibility to anodic oxidation. Figure 4 shows IR-compensated CVs recorded on the four electrodes. The current-potential profiles, Fig. 4a, are similar on all four electrodes but the current densities recorded differ considerably especially at the anodic and cathodic limits of the scan. The expanded sections in Fig. 4b show that the distinct stages of oxidation/reduction observed differ in current density on the four electrodes. The more erratic current observed on the $UO_{2.002}$ electrode can be attributed to the greater difficulty in applying the IR compensation to this electrode which has a resistance $\sim 10^2$ that of the other three electrodes. At the cathodic limit of the scan the currents can be attributed to H_2O reduction to H_2. The very high current for this reaction on the SIMFUEL electrode, Fig. 4, has been shown to be due to the catalysis of this reaction on the noble metal particles present in this material. While considerably lower than on SIMFUEL, the heavily-doped Dy-UO_2 and undoped $UO_{2.002}$ electrode supports a measurably higher current for this reaction than the Gd-UO_2 electrode.

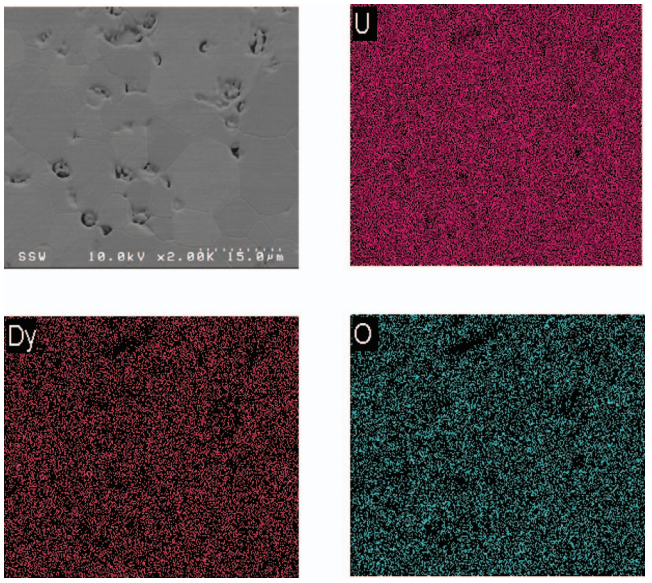

Figure 3. EDX maps recorded on a Dy-doped UO_2 at a magnification of 2000X.

In the potential range $-0.8\ V \leq E \leq -0.4\ V$ (region I, Fig. 4b) no significant oxidation current was observed on any electrode. In previous studies, current in this potential range has been attributed to the oxidation of hyperstoichiometric (UO_{2+x}) surface sites.[27,34]

Over the potential range $-0.4\ V \leq E \leq 0.0\ V$ (region II), a shallow increase in anodic current is observed on the $UO_{2.002}$ and SIMFUEL electrodes and, to a lesser degree, on the Dy-UO_2 electrode. No significant current increase is observed on the Gd-UO_2 electrode. The current increase commences for $E \geq -0.4$ V. Anodic oxidation in this region has been studied extensively on 1.5 at% SIMFUEL and surface oxidation clearly demonstrated by X-ray photoelectron spectroscopy.[27] Oxidation involves the incorporation of O^{2-} ions into interstitial sites in the stoichiometric UO_2 lattice (i.e., the creation of O interstitial ions, O_i) accompanied by the conversion of U^{IV} to U^{V}. Oxidation at these locations yields a surface layer of $U^{IV}{}_{1-2x}U^{V}{}_{2x}O_{2+x}$ with a thickness limited by diffusion of O to sub-surface locations. Although difficult to demonstrate, it has been claimed that the limiting composition of the UO_{2+x} surface is $UO_{2.33}$.[34] On hyperstoichiometric surfaces oxidation in this region, which commences in region I, can be extensive since O^{2-} diffusion to sub-surface locations is facilitated.[35]

The very low currents observed, on the more reactive $UO_{2.002}$ and SIMFUEL, are consistent with these electrodes being close to stoichiometric. This can be appreciated by comparing the anodic currents in this region to those observed on non-stoichiometric UO_2-Y_2O_3 electrodes.[36] However, currents on $UO_{2.002}$ are marginally higher than those recorded on the SIMFUEL due to the slight non-stoichiometry present in this electrode.[7] For the four electrodes investigated, the currents in this potential region are in the order

$$UO_{2.002} > \text{SIMFUEL} > Dy - UO_2 > Gd - UO_2 \qquad [2]$$

For the potential range $0.0\ V \leq E \leq 0.3\ V$ (region III) the anodic current increases markedly on $UO_{2.002}$, SIMFUEL and Dy-UO_2 but only slightly on Gd-UO_2. This increase has been shown to be due to the onset of U^{VI} formation and dissolution as $UO_2{}^{2+}$.[34] In the neutral to slightly alkaline solutions employed in these experiments, the U^{VI} accumulates on the electrode surface as $UO_3.yH_2O$, although dissolution can be maintained by a decrease in pH as a consequence of U^{VI} hydrolysis as the current increases at potentials $> +0.3$ V.[37] The order of reactivity in this potential range is the same as at the lower potentials. This is not surprising since the formation of UO_{2+x} is a precursor to the formation of U^{VI},

$$UO_2 \rightarrow UO_{2+x} \rightarrow UO_{3.y}H_2O/UO_2^{2+} \qquad [3]$$

In this regard electrochemical oxidation in an aqueous environment follows a similar sequential process to that observed in air oxidation. Figure 5 compares the currents recorded at 0 V and 0.3 V for all four electrodes (i.e., the first and second steps, respectively, in equation 3).

On the reverse scan the extent of oxidation of the electrodes can be gauged by the size of the reduction peak in region IV. This peak has been shown to be due to the cathodic reduction of the $UO_{2+x}/UO_3.yH_2O$ surface oxidation products. On $UO_{2.002}$ the extent of surface reduction, indicated by the charge associated with

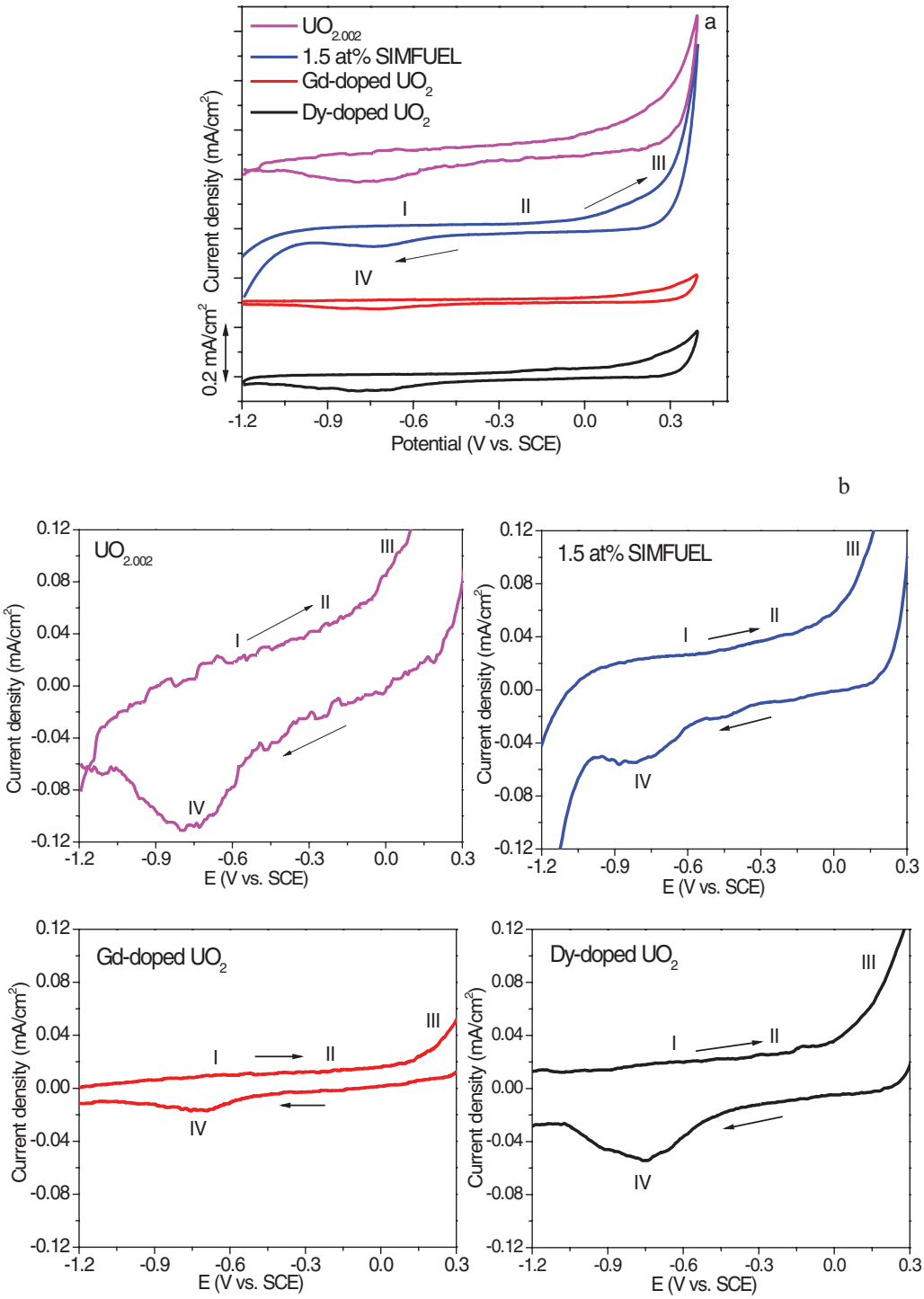

Figure 4. CVs recorded on $UO_{2.002}$, 1.5 at% SIMFUEL Gd-doped UO_2, and Dy-doped UO_2 electrodes in an Ar-purged 0.1 mol.L^{-1} NaCl solution (pH = 9): (a) scans are offset by 0.2 mA cm^{-2} and (b) individual scans. The scan rate = 10 mV.s^{-1}.

the reduction peak, is the highest. This indicates a more extensive UO_2 matrix oxidation and conversion to U^{VI} attributable to the slight non-stoichiometry present in this electrode.[7] For, SIMFUEL and Dy-UO_2 the reduction charge is approximately the same, although the reduction process is partially obscured on the SIMFUEL by the H_2O reduction current. By comparison, the extent of oxidation of the Gd-UO_2 electrode is minor, as expected considering the very small anodic oxidation currents measured on this electrode.

Considering the large difference in anodic currents observed at E > 0.1 V, the similarity in the extent of oxidation of SIMFUEL and Dy-UO_2 is surprising. A possibility is that both electrodes experience a similar degree of oxidation to the UO_{2+x} stage, but the subsequent oxidation to U^{VI} is inhibited on the Dy-UO_2 electrode leading to a lower anodic dissolution current but a similar degree of surface oxidation compared to SIMFUEL. In the absence of surface analytical evidence this claim is unproven.

Based on these results, the anodic reactivity is in the order noted in equation 2. Since three of the electrodes are RE^{III}-doped, the small extent of anodic oxidation on these electrodes is consistent with the expectation from air oxidation results that the reactivity will be lim-

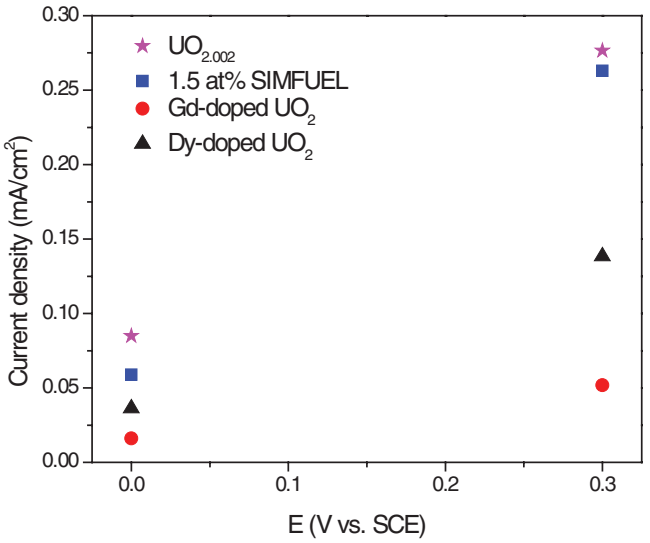

Figure 5. Anodic currents recorded at 0 and 0.3 V on four UO_2 electrodes in Ar-purged 0.1 mol.L^{-1} NaCl solution (pH = 9).

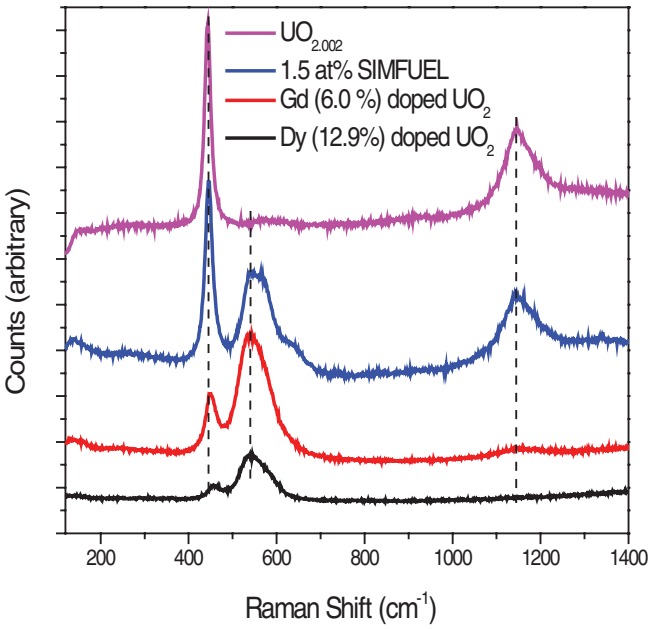

Figure 6. Raman spectra recorded on four freshly polished UO_2 electrodes.

ited. However, the expectation that the extent of oxidation will be proportional to the total RE^{III} content is not borne out, since the more heavily doped Dy-UO_2 electrode is more extensively oxidized than the Gd-UO_2 electrode.

Raman analyzes.— Raman spectroscopy has been commonly used to investigate the structure of the U-O system.[6,8,9] Uranium dioxide has a cubic fluorite structure and belongs to the space group O_h ($Fm3m$)[38] and should exhibit two vibrational modes; i.e., a Raman-active phonon (T_{2g}) and an infrared-active phonon (T_{1u}).[39] This structure possesses six optical-phonon branches which show three zone-center frequencies i.e 278 cm^{-1}, 445 cm^{-1} and 578 cm^{-1} corresponding to the doubly degenerate IR active (T_{1u}) TO mode, the triply degenerate Raman active (T_{2g}) mode, and the nondegenerate IR active (T_{1u}) LO mode. Therefore, Raman scattering for pure UO_2 should generate a fundamental vibrational stretch at ~ 445 cm^{-1} and a second band at ~ 1150 cm^{-1}. The 445 cm^{-1} band is ascribed to the symmetric stretching mode which arises due to oxygen breathing vibrations around U^{IV} in the fluorite structure. The second band at ~ 1150 cm^{-1} was initially reported by Graves[39] on single crystal UO_2 and by Schoenes and Manara[40,41] on polycrystalline UO_2 using a similar source (514 nm laser) and attributed to a crystal field transition ($\Gamma_5 \rightarrow \Gamma_3$) (for the quasi-perfect fluorite structure). More recently this band has been reassigned as an overtone (2L-O) of the first order L-O phonon (575 cm^{-1}).[42] Manara et al.[41] claimed this band can be taken as a fingerprint for the quasi-perfect fluorite structure and showed that its intensity decreased considerably as the defect structure due to increasing non-stoichiometry developed. This assignment was recently confirmed by He et al.[8]

Raman spectra recorded on the four electrodes are shown in Fig. 6. While all four exhibit similar structure, the relative peak intensities differ considerably. A number of general features can be noted:

(i) For the RE^{III}-doped electrodes, no peaks indicating the presence of Gd_2O_3 or Dy_2O_3 are observed. For the cubic Gd_2O_3, peaks at 375 cm^{-1} and 480 cm^{-1}, due to the basic vibrational modes, would be expected. Their absence confirms the RE^{III} cations are in solid solution within the UO_2 matrix.

(ii) The two bands associated with the fluorite lattice at 445 cm^{-1} and 1150 cm^{-1} decrease in intensity in the order $UO_{2.002}$ > SIMFUEL > Gd-UO_2 > Dy-UO_2; i.e., as the overall extent of RE^{III}-doping increases.

(iii) The peak at 445 cm^{-1} shifts to a higher wavelength and appears to develop asymmetry on the high wavenumber side.

(iv) The broad band in the region 500 to 700 cm^{-1} becomes dominant as the doping level increases and its structure changes considerably.

(v) The intensity of the small peak at ~ 155 cm^{-1} decreases with increasing doping level.

$UO_{2.002}$.—The Raman spectrum for $UO_{2.002}$, Fig. 6, is consistent with the literature[6,9] and exhibits a sharp peak at 445 cm^{-1} and a broad one at 1150 cm^{-1}, as expected for close to stoichiometric UO_2.[9] The multi-component broad band in the 500–700 cm^{-1} region and the small peak at 155 cm^{-1}[19,38] are not present indicating the UO_2 lattice does not contain significant defects and distortions.

SIMFUEL.—Raman and XRD analyses on a range of SIMFUELs (1.5 at%, 3.0 at% and 6.0 at%) have been reported.[6] The XRD diffraction patterns indicated a decrease in UO_2 lattice constant with an increase in simulated burn-up consistent with published literature. However, whether or not this can be attributed to rare earth doping alone is dubious since the influence of dopants on the UO_2 lattice parameter has been shown to vary with the identity of the dopant. Kapoor et al[43] observed a decrease in lattice constant when the dopant was Gd, whereas Wilson et al[44] reported an increase with La. In addition, the presence of Zr in these SIMFUELs would be expected to have an over-riding influence on the lattice constant.[6] The Raman spectrum recorded on the SIMFUEL shows the presence of both the peaks at 445 and 1150 cm^{-1} similar to near stoichiometric UO_2, with the band at 1150 cm^{-1} being comparatively weak compared to that at 445 cm^{-1} consistent with a distortion of the cubic fluorite lattice.

The broad band between 500–700 cm^{-1} observed here on the 1.5 at% SIMFUEL was attributed to UO_2 lattice damage, due to the formation of defects caused by doping. Previously, a broad band centered at 585 cm^{-1} observed on single crystal UO_2 was deconvoluted into bands at 578 and 640 cm^{-1}.[38] The band at 578 cm^{-1} has been attributed to the longitudinal optical (LO) component of the T_{1u} mode which arises due to the crystal lattice disorder whereas the band at 640 cm^{-1} (observed at 630 cm^{-1})[9] has been attributed to distortion of the anion sublattice[8] and more recently attributed to a vibrational mode involving atoms in clusters of interstitial O atoms.[9]

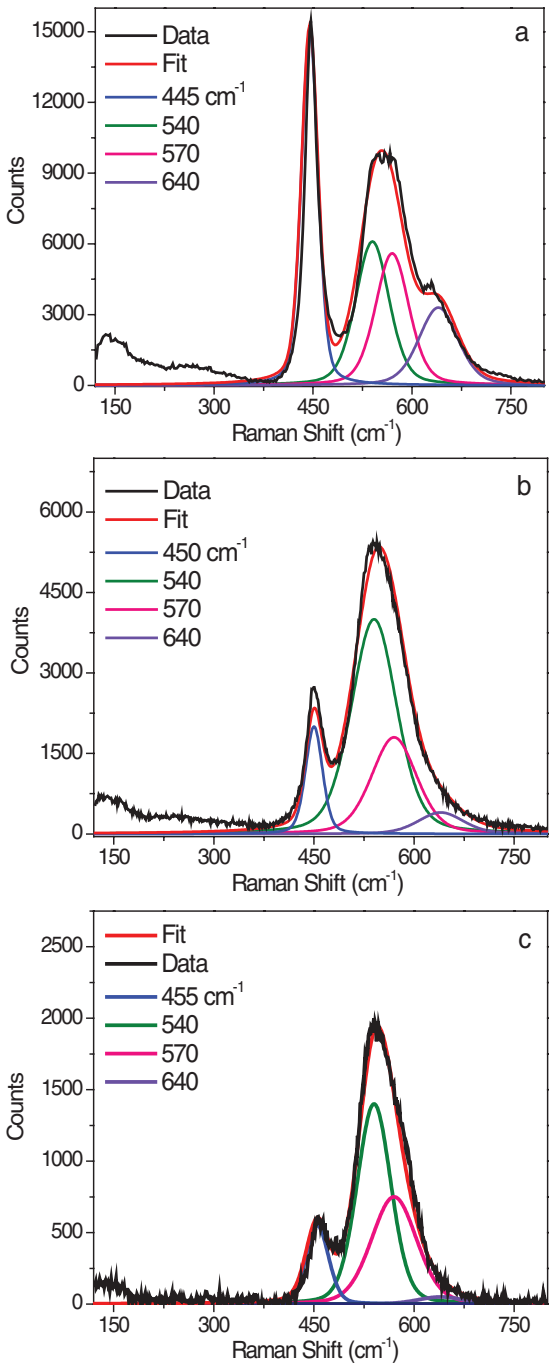

Figure 7. Raman spectra recorded on (a) 1.5 at% SIMFUEL (b) Gd-doped UO_2 (c) Dy-doped UO_2 electrodes and deconvoluted into contributions from bands at ~450, 540, 570 and 640 cm^{-1}.

Based on these considerations, this broad band for 1.5 at% SIMFUEL was deconvoluted into three peaks at ~ 540, 570 and 640 cm^{-1}, Fig. 7a. The peak at 570 cm^{-1} was shown to be independent of doping level in the series of SIMFUELs investigated previously[6] and is associated with the close-to-perfect fluorite structure.[8] While previously observed in the series of SIMFUELs the peak at 540 cm^{-1} was unassigned although it was tentatively suggested it could be attributed to the formation of a phase with a perovskite (ABO_3) structure.[6] While this may have been a possibility in SIMFUELs containing dopants such as Ba and Sr (able to occupy A sites) and Zr (B sites), it is highly unlikely in a matrix containing only RE^{III} cations. The prominent peak at 640 cm^{-1} has been associated with the cuboctahedra constituting the U_4O_9 phase[8,9] and would not be expected in this stoichiometric SIMFUEL. A new assignment for this peak will be offered below.

Gd-UO_2.—For the Gd-UO_2 specimen the intensity of the peak at 450 cm^{-1} is considerably lower than observed on the SIMFUEL and, especially, $UO_{2.002}$, and the band at 1150 cm^{-1} is very weak confirming the degradation of the fluorite structure due to doping, Fig. 6. Relative to these two peaks, the broad band in the 500 to 700 cm^{-1} wavelength region becomes more intense than observed for SIMFUEL.

Deconvolution of this region shows that the peak at 540 cm^{-1} dominates over those at 570 cm^{-1} and 640 cm^{-1}, Fig. 7b. As noted above, the peak at 540 cm^{-1} is not observed in undoped UO_2. However, a peak at ~ 560 cm^{-1}, observed on RE^{III}-doped (Gd, La, Pr, Nd, Eu) CeO_2 (which has a similar fluorite lattice to UO_2) has been attributed to the creation of oxygen vacancies (O_V).[45] The presence of such vacancies in UO_2 would be consistent with the calculations of Park and Olander,[21,22] and the observations of Desgranges et al[25] who attributed a peak at this wavenumber (recorded on Nd-doped UO_2) to a local phonon mode associated with Ov-induced lattice distortion. The dominance of this peak in Gd-UO_2 confirms that the primary influence of RE^{III}-doping is the creation of O_V due to the need for charge compensation. Only a very small peak is observed at 640 cm^{-1} confirming the absence of any clustering of O_I associated with excess O in the oxide. Whether or not the electrode contains the second phase involving U^V formation and free of lattice distortions cannot be determined without a more detailed Raman mapping of the electrode surface.

Dy-UO_2.—For the Dy-UO_2 electrode the peak at 1150 cm^{-1} is effectively absent and the broad band between 500 cm^{-1} and 700 cm^{-1} becomes even more dominant over the T_{2g} band, Fig. 6. Inspection of the T_{2g} band shows a shift to higher frequencies (445 cm^{-1} to 455 cm^{-1}) and a Fano-type, rather than Lorentzian, line shape. Such a shift has been variously interpreted. For the RE^{III}-doped CeO_2 this shift was attributed to the increasing presence of O_V,[46] whereas for non-stoichiometric UO_2 a similar shift was attributed to the clustering of O_I due to cuboctahedral formation as UO_2 converted to U_4O_9.[9] For high degrees of non-stoichiometry this broadened peak could be deconvoluted into peaks at 445 cm^{-1} and a second peak at 470 cm^{-1},[8] which was shown to be a characteristic feature of the distortion to a tetragonal phase.

Deconvolution of the broad band between 500 cm^{-1} and 700 cm^{-1} yields the same three peaks observed for Gd-UO_2 with the peak at 540 cm^{-1} dominant, Fig. 7c. The ratio of the intensities of the 540 cm^{-1} and 570 cm^{-1} peaks is approximately the same as for Gd-UO_2, and the peak at 640 cm^{-1} is effectively absent.

General Raman features.—Figure 8 shows the ratio between the areas of the T_{2g} peak (445 cm^{-1}) and the peak at 540 cm^{-1}. Since the T_{2g} peak is characteristic of the undisturbed fluorite lattice and the 540 cm^{-1} peak is attributed to the creation of O_V associated with the RE^{III} dopant, the ratio of these two peaks is commonly taken as a measure of the number of such vacancies.[47,48] The ratio changes in the sequence.

$$\text{SIMFUEL} > \text{Gd-}UO_2 \sim \text{Dy-}UO_2 \qquad [4]$$

A second feature worth noting is that the decrease in intensity of the minor broad peak around 155 cm^{-1} follows this same sequence. This peak has been related to the change in unit cell size in U_4O_9[9] and, by comparison to ZrO_2 spectra, to a distortion of the U sublattice associated with the transition to tetragonal U_3O_7.[8] Some XRD evidence was offered in support of this claim. Although a peak in this wavelength range cannot be attributed to the presence of the significant amounts of O_I that would be required to form U_4O_9/U_3O_7, the loss of intensity suggests a decreasing tendency to form the distorted structures associated with the clustering of O_I ions.

General XPS features.— Figure 9 shows fitted and deconvoluted U4f spectra for two of the freshly polished electrodes ($UO_{2.002}$ and Gd-UO_2). Similar spectra were obtained for the other two electrodes. These spectra serve to characterize the surface properties of the

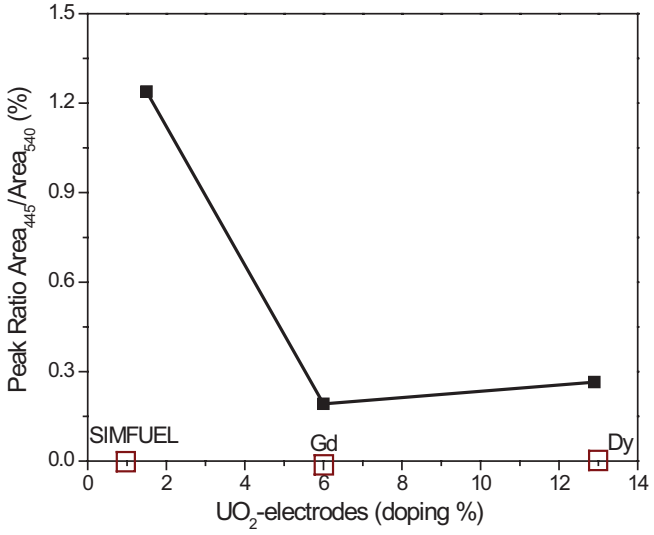

Figure 8. The area ratio of the Raman peaks recorded ~ 445 cm^{-1} and 540 cm^{-1} (A_{445}/A_{540}: Figure 7) as a function of doping level.

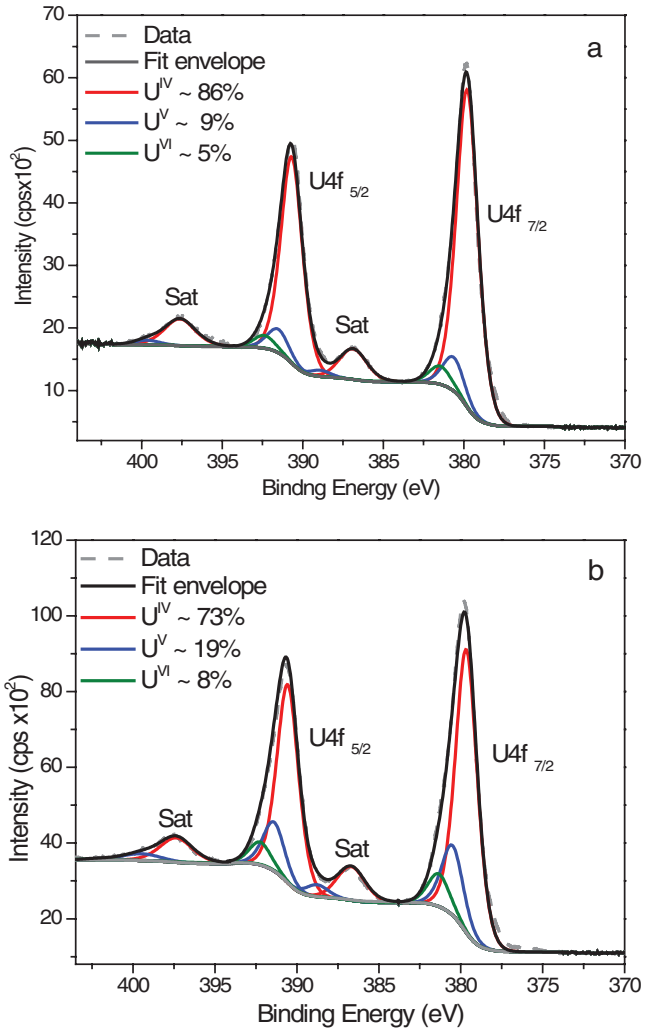

Figure 9. U 4f spectrum recorded on (a) $UO_{2.002}$ (b) Gd-doped UO_2 and resolved into contributions from U^{IV}, U^V and U^{VI} species.

Table I. Relative fractions of U oxidation states in the surface of all four electrodes obtained after deconvolution of U 4f spectra.

	Surface fractions		
Specimen	U^{IV} (%)	U^V (%)	U^{VI} (%)
$UO_{2.002}$	86	9	5
SIMFUEL	86	8	6
Gd-UO_2	73	19	8
Dy-UO_2	76	12	12

electrodes. Table I shows the relative surface fractions of U^{IV}, U^V and U^{VI}. The distribution of oxidation states in the surfaces of the $UO_{2.002}$ and SIMFUEL electrodes are similar suggesting that light RE^{III} doping (up to 1.5 at%) does not significantly perturb the surface composition consistent with the similar electrochemical reactivities observed on these two electrodes, Fig. 4.

The two RE^{III} doped electrodes exhibit higher U^V and U^{VI} contents. This difference between the Gd-UO_2/Dy-UO_2 and $UO_{2.002}$/SIMFUEL electrodes is significant and not simply due to the slight air oxidation on the short, but inevitable, exposure to air when the specimen is transferred from the electrochemical cell to the spectrometer. An increase in U^V content accompanied by increased non-stoichiometry has been shown to lead to increased electrochemical reactivity,[7,35] but the opposite is observed for the Gd-UO_2/Dy-UO_2 electrodes, the reactivity decreasing with RE^{III}, Fig. 4. The relatively small changes in U^V content of the Gd-UO_2 and Dy-UO_2 surfaces suggest that charge compensation on the electrode surfaces (on introducing RE^{III}) is most likely due to the enhanced concentration of O_V as indicated by the Raman analyses. It is also possible this slight enhancement reflects the presence of the second $U^VRE^{III}O_2$ phase described by Desgranges et al.[25] Whether or not the higher U^V in the Gd-UO_2 surface compared to that in the Dy-UO_2 surface accounts for the extremely low electrochemical reactivity of this electrode, Fig. 4, cannot be confirmed based on the small compositional difference observed, Table I.

Discussion

The plots in Fig. 4 show the influence of the changes in electrode composition on the anodic oxidation reaction. At a potential of 0 V, the electrode would be expected to be oxidized to UO_{2+x}[27] and the current to reflect, approximately, the rate and extent of the first step in equation 3 ($UO_2 \rightarrow UO_{2+x}$). At 0.3 V, the currents would be representative of the rate of the second step ($UO_{2+x} \rightarrow UO_3.yH_2O/UO_2^{2+}$). While this separation is somewhat arbitrary, it can be used to illustrate the influence of doping on both stages of the surface oxidation / conversion / dissolution reaction. In this regard electrochemical oxidation in an aqueous environment follows a similar two step reaction sequence to that observed for air oxidation.

Based on the Raman and XPS analyses, the lower electrochemical reactivity of the two RE^{III}-doped electrodes compared to the $UO_{2.002}$ and SIMFUEL electrodes can be related to their tendency to form RE^{III}-O_V clusters. Both electrodes show a strong Raman peak at 540 cm^{-1} which, by comparison to the spectra observed for RE^{III}-doped CeO_2, can be attributed to the formation of O vacancies (Ov) in response to the need for charge compensation. This is partially supported by the XPS results which exhibit only minor variations in surface composition (U^{IV}, U^V, U^{VI}) as a function of dopant level. This leads to the formation of RE^{III}-O_V clusters which limits the number of available O_V sites required for the incorporation of O during anodic oxidation. This is consistent with the calculations of Park and Olander[22] which show that the formation of Gd^{III}-O_V clusters does not increase the number of extrinsic vacancies but diminishes already existing ones.

This effect is compounded by the influence of doping on the fluorite lattice parameter. For CeO_2, the cation radii for RE dopants (e.g., La^{III}, Eu^{III}, Gd^{III}) are generally greater than that of the matrix

cation (Ce^{IV}).[49] This leads to an increase in lattice parameter which expands the fluorite lattice and facilitates the incorporation of O^{2-} and increases its mobility within the lattice. This enhances the catalytic capability of the oxide and improves its ability to act as a high temperature oxygen anion conductor in solid oxide fuel cells.[50]

By contrast the ionic radius of U^{IV} is approximately the same as that of Gd^{III}, and a similar influence of doping on lattice parameter would not necessarily be expected. However, there is considerable XRD evidence to show that, due to RE^{III}-O_V clustering, Gd doping causes a lattice contraction in UO_2,[13,43] which would lead to a decreased mobility of O^{2-} ions within the doped UO_2 matrix. Since the initial step in the anodic oxidation reaction ($UO_2 \rightarrow UO_{2+x}$) involves the incorporation of O^{2-} ions into O_V in the fluorite lattice, these effects would be expected to limit the anodic oxidation rate as indicated by the small amount of cathodic charge required to reduce the film formed, Figs. 4 and 5.

The more heavily doped Dy-UO_2 would be expected to be even less reactive than the Gd-UO_2 if anodic reactivity was controlled solely by the influence of RE^{III}-O_V clustering. However, the electrochemical behavior (Figs. 4 and 5) does not support this, the Dy-UO_2 being more reactive for both stages of anodic oxidation, reaction 3. The ionic radius of Dy is slightly less than that of Gd making it more incompatible with the UO_2 matrix. The low intensity of the 455 cm^{-1} peak and the total absence of the 1150 cm^{-1} peak confirm the greater extent of disorder in the Dy-UO_2 electrode compared to the other two electrodes but provide no detailed explanation for this decreased reactivity.

Andersson et al[51] studied the influence of different trivalent dopants on the ionic conductivity of O ions in CeO_2 and predicted that the optimum dopant combinations to improve conductivity, and hence catalytic activity, would be Nd/Sm and Pr/Gd. While this is the opposite influence to the decreased ionic conductivity required to suppress UO_2 oxidation, similar calculations and/or experimental data would be required if the difference in susceptibility to anodic oxidation due to RE^{III}-doping is to be more clearly understood.

While the number of dopant-vacancy clusters in SIMFUEL, as indicated by the ratio A_{455}/A_{540} (Fig. 8), is consistent with the higher anodic reactivity of this electrode, Figs. 4 and 5, a number of ambiguities exist, in particular the origin of the Raman peak at 640 cm^{-1}. As noted above, a peak around this wavelength has been assigned to the presence of the cuboctahedral clusters associated with the presence of U_4O_9. However, the presence of such clusters is associated with a much higher anodic reactivity than observed on the 1.5 at% SIMFUEL used in this study.[52,53]

The previous study with SIMFUELs showed that this peak at 640 cm^{-1} increased in relative intensity while that for the peak at 540 cm^{-1} decreased[6] as the degree of simulated burn-up (increase in doping level) was increased. This decrease in relative intensity of the 540 cm^{-1} peak suggests the number, or at least the relative importance, of RE^{III}-O_V clusters, is decreasing despite the increase in RE^{III} content. However, this decrease is accompanied by the decrease in lattice parameter expected as RE^{III} doping increases. The SIMFUEL contains primarily La^{III}, Nd^{III} and Y^{III}. While Y^{III} has an ionic radius close to that of U^{IV} the two RE^{III} cations have considerable larger radii than that of Gd^{III}. Consequently, it is possible they might not be as effective as Gd^{III} in forming RE^{III}-O_V clusters.

Irrespective of this influence, this does not explain the greater importance of the peak at 640 cm^{-1} as the doping content increases. As noted above, the SIMFUEL also contains Zr^{IV}, the content of which also increases as the degree of simulated burn-up increases. The cation, Zr^{IV}, has an ionic radius significantly less than that of U^{IV} and because of this size, differential exerts a large, effectively controlling, influence on the lattice dimensions of irradiated nuclear fuel[6] [and references therein]. It is likely, therefore, that the decrease in lattice parameter observed in the sequence of SIMFUELs[6] can be attributed primarily to the presence of Zr^{IV} rather than that of the RE^{III} dopants.

If this is the case, then it suggests a different assignment of the peak at 640 cm^{-1} in the Raman spectrum. In CeO_2, the presence of Zr^{IV} leads to the formation of defects with O_h symmetry in which the Zr^{IV} cation is in 8-fold coordination with O^{2-} (a Zr-O_8-type complex). This complex forms as a consequence of the difference in ionic radii between Zr^{IV} and the host matrix Ce^{IV} cation and contains a very limited concentration of O_V.[45,54] CeO_2 doped only with Zr^{IV} yields a Raman peak around 600 to 620 cm^{-1}.[45] However, in CeO_2 doped with both Zr^{IV} and RE^{III} cations, peaks at 560 cm^{-1}, attributed to the formation of O_V due to the RE^{III}-doping, and this peak at 600–620 cm^{-1} are both observed. A similar influence of Zr^{IV} in UO_2 could account for the Raman peak at 640 cm^{-1} in the SIMFUEL electrode, Fig. 7a. Since Zr^{IV} doping also leads to a decrease in lattice parameter it would be expected to stabilize the UO_2 lattice against anodic oxidation and, by analogy, air oxidation.

Conclusions

Two RE^{III}-doped UO_2 electrodes, an undoped and a lightly doped SIMFUEL (1.5 at%) have been characterized by Raman spectroscopy, XPS and cyclic voltammetry. The electrochemical reactivity decreased in the order UO_2 > SIMFUEL > Dy-UO_2 > Gd-UO_2. While this sequence shows a decrease in reactivity with increase in RE^{III} doping, the reactivity is not directly related to the RE^{III} content suggesting a presently unknown influence of either the nature of the dopant or the overall extent of doping.

Voltammetry shows that doping suppresses both stages of anodic oxidation; matrix oxidation ($UO_2 \rightarrow UO_{2+x}$) and its further oxidation to soluble U^{VI} (as UO_2^{2+}). The second step appears to be more influenced than the first. This is consistent with the influence of RE^{III} doping on the kinetics of air oxidation which also proceeds in two stages ($UO_2 \rightarrow U_3O_7/U_4O_9 \rightarrow U_3O_8$).

Raman spectroscopy shows the structure becomes increasingly dominated by the presence of RE^{III}-O_V clusters as the doping level increases. This decreases the number of O_V available to accommodate the injection of the O_I required for oxidation to occur.

The Raman spectra recorded on the SIMFUEL suggests the behavior of this matrix is strongly influenced by the lattice contraction caused by the formation of Zr-O_8 clusters. The influence of these clusters on the reactivity of the UO_2 matrix remains to be characterized.

Acknowledgments

This research is funded under the Industrial Research Chair agreement between the Canadian Natural Sciences and Engineering Research Council (NSERC) and Nuclear Waste Management Organization (NWMO), Toronto, Canada. Surface Science Western is gratefully acknowledged for the use of their Raman, XPS and SEM equipment.

References

1. Nuclear Waste Management Organization (NWMO). Choosing a Way Forward: The Future Management of Canada's Used Nuclear Fuel. (Available at www.nwmo.ca) (2005).
2. F. King and M. Kolar, Ontario Power Generation Report, 06819-REP-01200-10041-R00, Toronto (2000).
3. L. H. Johnson, D. M. LeNeveu, F. King, D. W. Shoesmith, M. Kolar, D. W. Oscarson, S. Sunder, C. Onofrei, and J. L. Crosthwaite, *Atomic Energy of Canada Limited Report*, 11494-2, COG-95-552-2 (1996).
4. R. Guillamont, R. T. Fanghanel, I. Grenthe, V. Neck, D. Palmer, M. H. Rand, and M. H. OECDNEA, *Chemical Thermodynamics*, **5**,182 (2003).
5. D. W. Shoesmith, in *Uranium Cradle to Grave*, P. Burns and G. E. Sigmon, Editors, 43, Notre Dame (2013).
6. H. He, P. G. Keech, M. E. Broczkowski, J. J. Noel, and D. W. Shoemsith, *Can. J. Chem.*, **85**, 1 (2007).
7. H. He, M. Broczkowski, K. O'Neil, D. Ofori, O. Semenikhin, and D. W. Shoesmith, *Nuclear Waste Management Organization*, NWMO TR-2012-09 Toronto, (2012).
8. H. He and D. Shoesmith, *Phys. Chem. Chem. Phys.*, **12**, 8108 (2010).
9. L. Desgranges, G. Baldinozzi, P. Simon, G. Guimbretière, and A. Canizares, *J. of Raman Spectrosc.*, **43**, 455 (2012).
10. R. J. McEachern and P. Taylor, *J. Nucl. Mater.*, **254**, 87 (1998).
11. L. E. Thomas, R. E. Einziger, and H. C. Buchanan, *J. Nucl. Mater.*, **201**, 310 (1993).

12. Y. K. Ha, Y. H. Cho, J. G. Kim, K. Y. Jee, and W. H. Kim, *Recent Advances in Actinide Science*, I. L. May, N. D. Bryan, and R. Alvares, Editors, United Kingdom (2006).
13. J. G. Kim, Y. K. Ha, S. D. Park, K. Y. Jee, and W. H. Kim, *J. Nucl. Mater.*, **297**, 327 (2001).
14. K. Park, M. S. Yang, and H. S. Park, *J. Nucl. Mater.*, **247**, 116 (1997).
15. P. G. Boczar, J. Griffiths, and I. J. Hastings, in *Impact of Extended Burnup on the Nuclear Fuel Cycle*, *Proceedings of an Advisory Group Meeting, IAEA-TECDOC-699*, Vienna (1991).
16. K. Hesketh, in *Impact of Extended Burnup on the Nuclear Fuel Cycle*, *Proceedings of an Advisory Group Meeting, IAEA-TECDOC-699*, Vienna (1991).
17. P. G. Lucuta, R. A. Verrall, H. Matzke, and B. J. Palmer, *J. Nucl. Mater.*, **178**, 48 (1991).
18. J. Cobos, D. Papaioannou, J. Spino, and M. Coquerelle, *J. Alloys Compd.*, **271-273**, 610 (1998).
19. R. E. Einziger, L. E. Thomas, H. C. Buchanan, and R. B. Stout, *J. Nucl. Mater.*, **190**, 53 (1992).
20. K. M. Wasywich, W. H. Hocking, D. W. Shoesmith, and P. Taylor, *Nucl. Technol.*, **104**, 309 (1993).
21. K. Park and D. R. Olander, *High Temp. Sci.*, **29**, 203 (1990).
22. K. Park and D. R. Olander, *J. Nucl. Mater.*, **187**, 89 (1992).
23. T. Ohmichi, S. Fukushima, A. Maeda, and H. Watanabe, *J. Nucl. Mater.*, **102**, 40 (1981).
24. T Fujino, K. Ouchi, Y. Mozumi, R. Ueda, and H. Tagawa, *J. Nucl. Mater.*, **174**, 92 (1990).
25. L. Desgranges, Y. Pontillon, P. Matheron, M. Marcet, P. Simon, G. Guimbretiere, and F. Porcher, *Inorg. Chem.*, **51**, 9147 (2012).
26. D. W. Shoesmith, *Nuclear Waste Management Organization Report TR-2007-03* Toronto (2007).
27. B. G. Santos, H. W. Nesbitt, J. J. Noel, and D. W. Shoesmith, *Electrochim. Acta*, **49**, 1863 (2004).
28. M. Razdan, D. S. Hall, P. G. Keech, and D. W. Shoesmith, *Electrochim. Acta*, **83**, 410 (2012).
29. M. Schindler, F. C. Hawthorne, M. S. Freund, and P. C. Burns, *Geochim. Cosmochim. Acta*, **73**, 2471 (2009).
30. E. S. Ilton, A. Haiduc, C. L. Cahil, and A. R. Felmy, *Inorg. Chem. Commun.*, **44**, 2986 (2005).
31. E. S. Ilton, J. F. Boily, and P. S. Bagus, *Surf. Sci.*, **601**, 908 (2007).
32. D. W. Shoesmith, *Nuclear Waste Management Organization Report TR-2008-19*, Toronto (2008).
33. M. E. Broczkowski, P. G. Keech, J. J. Noël, and D. W. Shoesmith, *J. Electrochem. Soc.*, **157**, C275 (2010).
34. D. W. Shoesmith, *J. Nucl. Mater.*, **282**, 1 (2000).
35. H. He, PhD Thesis, in Chemistry, Western University, London, Ontario (2010).
36. M. Razdan, PhD Thesis, in Chemistry, Western University, London, Ontario (2013).
37. B. G. Santos, J. J. Noël, and D. W. Shoesmith, *Electrochim. Acta*, **51**, 4157 (2006).
38. S. D. Senanayake, R. Rousseau, D. Colegrave, and H. Idriss, *J. Nucl. Mater.*, **342**, 179 (2005).
39. P. R. Graves, *Appl. Spectrosc.*, **44**, 1665 (1990).
40. J. Schoenes, *J. Chem. Soc.*, **83**, 1205 (1987).
41. D. Manara and B. Renker, *J. Nucl. Mater.*, **321**, 233 (2003).
42. T. Livneh and E. Sterer, *Phys. Rev. B*, **73**, 0851181 (2006).
43. K. Kapoor, S. V. Ramana Rao, S. T. Sanyal, and A. Singh, *J. Nucl. Mater.*, **321**, 331 (2003).
44. W. B. Wilson, C. A. Alexander, and A. F. Gerds, *J. Inorg. Nucl. Chem.*, **20**, 242 (1961).
45. L. Li, F. Chen, J. Q. Lu, and M. F. Luo, *J. Phys. Chem. A*, **115**, 7972 (2011).
46. J. R. McBride, K. C. Hass, B. D. Poindexter, and W. H. Weber, *J. Appl. Phys.*, **76**, 2435 (1994).
47. Z. Y. Pu, J. Q. Lu, M. F. Luo, and Y. L. Xie, *J. Phys. Chem. C*, **111**, 18695 (2007).
48. H. Bao, X. Chen, J. Fang, Z. Jiang, and W. Huang, *Catal. Lett.*, **125**, 160 (2008).
49. W. Y. Hernandez, O. H. Laguna, M. A. Centeno, and J. A. Odriozola, *J. Solid State Chem.*, **184**, 3014 (2011).
50. H. Yokokawa, T. Horita, N. Sakai, K. Yamaji, M. E. Brito, Y. P. Xiong, and H. Kishimoto, *Solid State Ionics*, **177**, 1705 (2006).
51. D. A. Andersson, S. I. Simak, N. V. Skorodumova, I. A. Abrikosov, and B. Johansson, *Proceedings of the National Academy of Sciences*, **103**, 3518 (2007).
52. H. He, R. K. Zhu, Z. Qin, P. G. Keech, Z. F. Ding, and D. W. Shoesmith, *J. Electrochem. Soc.*, **156**, C87 (2009).
53. H. He, Z. Qin, and D. W. Shoesmith, *Electrochim. Acta*, **56**, 53 (2010).
54. M. F. Garcia, A. M. Arias, J. C. Hanson, and J. A. Rodriguez, *Chem. Rev.*, **104**, 4063 (2004).